

Effects of local rock heterogeneities on the hydromechanics of fractured rocks using a digital-image-based technique

W.C. Zhu^{a,b}, J. Liu^{a,*}, T.H. Yang^b, J.C. Sheng^a, D. Elsworth^c

^a*School of Oil and Gas Engineering, The University of Western Australia, WA 6009, Australia*

^b*Center for Rock Instability and Seismicity Research, Northeastern University, 110004 Shenyang, PR China*

^c*Department of Energy and Geo-Environmental Engineering, Penn State University, PA 16802, USA*

Accepted 21 March 2006

Available online 19 May 2006

Abstract

A digital-image-based (DIB) finite element approach is developed based on the numerical code rock failure process analysis (RFPA) to characterize micro-scale rock heterogeneity, and to understand the impact of micro-scale rock heterogeneity on the macro-scale hydromechanical response of rocks. The DIB technique incorporates small-scale spatial variability of initial deformation modulus, strength and permeability directly into a coupled hydromechanical model. Variability in Young's modulus, strength, and permeability is applied by a property map defined from the pixel-scale of a digital image. In the RFPA, mechanical deformation is followed, including the accumulation of damage applied in individual elements, which modifies modulus, strength, and permeability with the intensity of damage. The RFPA simulates progressive failure in fractured rocks, representing both the growth of existing fractures and the formation of new fractures, without having to identify crack tips and their interaction explicitly. In this DIB simulation approach, image voxels are used to give equivalent mechanical and flow properties. These property maps are ported to the model capable of solving directly for the evolving deformation, and fluid flow fields. The model is validated through comparisons of the simulated results with phenomenological observations documented in previous studies. The validated model is then applied to investigate the hydromechanical response of fractured rock characterized by digital image. The model is able to reproduce the spatial evolution of damage in the sample, the coalescence of existing cracks, and the formation of new cracks.

© 2006 Elsevier Ltd. All rights reserved.

Keywords: Rock; Heterogeneity; Coupled hydromechanics; Digital-image-based (DIB) technique; Failure process; Numerical simulation

1. Introduction

This study deals with the impact of local rock heterogeneities on the hydromechanics in the failure process of fractured rocks. Hydromechanical interactions are common in geological media because such media contain pores and fractures which can be fluid-filled and deformable [1–3]. When fractured rocks are damaged and fail under in situ conditions, the characterization of mechanical and transport properties presents a new challenge [4,5]. The scientific challenges are twofold: the first relates to how to characterize fractured rock at micro-scale, and the second

on how to translate that finely resolved characterization to reproduce the macro-scale hydromechanical response.

In previous studies, the heterogeneity and microstructures of rock materials have been characterized by using statistical tools including non-spatial and spatial statistics [5–10]. In these studies, including the one used previously in RFPA [5,10], the heterogeneity of rock is described by assigning different material properties to the microstructures (such as fractures) for which the constitutive laws are specified. These studies have demonstrated the importance of rock heterogeneity. However, these methods can misinterpret critical local-scale heterogeneities in the rock because it is usually difficult to adequately specify the statistical distribution parameters in order to reproduce real microstructures in rock. Therefore, these artificial internal heterogeneities or microstructure-based models

*Corresponding author. Tel.: +61 8 6488 7205.

E-mail address: jishan@cylle.uwa.edu.au (J. Liu).

may inadequately reflect the actual local geometrical and constitutive variations of microstructures in rocks.

Some recent studies have shown that digitized image data, such as the characteristics of different minerals and fractures in rocks, can be used to establish the level of heterogeneity. Digital image processing techniques are widely used in many areas of research and application such as in medical diagnosis, in the design of composite materials, and in concrete mechanics [11–14]. Digital image processing has been used in rock mechanics to detect discontinuity geometry in rock masses [15–18] and to analyze failure processes and fracture in rock [19]. Yue and his collaborators [20–22] have proposed a digital-image-based (DIB) numerical modeling method for the prediction of failure, which accounts for the actual mineral distribution in the rock.

In this study, we integrate DIB rock heterogeneity characterization directly into a well-established code RFPA for simulating the coupled hydromechanics of fractured rocks [10,23]. This integration is capable of predicting the macro-scale hydromechanical responses of fractured rocks, including the effects of the coalescence of existing cracks and the formation of new cracks, on flow rate, on stress re-distribution, and on localized deformation and progressive failure.

This paper aims at providing a new DIB technique to characterize the rock heterogeneity. The RFPA has been widely used as a numerical code to simulate the rock failure process under hydromechanical loading conditions, in this respect, the calibration is concentrated on capabilities of DIB technique in characterizing the rock heterogeneity. Moreover, the failure process of rock during hydromechanical process is modeled, and related mechanisms such as permeability and damage evaluation, are clarified.

2. Model description

Detailed descriptions of the coupled fluid flow, stress and damage model of RFPA has been presented previously [5,23]. This presentation includes a summary of the governing equations, a detailed description of the digital image processing technique, and a description of the implementation of DIB technique into RFPA.

2.1. Governing equations

The hydromechanics of saturated fractured rocks may be represented by two sets of governing equations: the fluid flow equation and the mechanical deformation and damage equation. These two sets of equations are linked through a number of cross-coupling relations.

2.1.1. Fluid flow equation

The governing equation for saturated fluid flow in porous medium is described by a liquid mass balance as

$$S_s \frac{\partial P}{\partial t} - \nabla \left[\frac{k \rho_l g}{\mu_l} (\nabla P - \rho_l g \nabla z) \right] = 0, \quad (1)$$

where P is the pore fluid pressure (Pa), ρ_l the liquid density (kg/m^3), μ_l the dynamic viscosity of the fluid (Pa s), t the time (s), k the permeability (m^2), g the acceleration due to gravity (m/s^2), z the vertical Cartesian coordinate (m), and S_s the specific storativity of the porous medium (1/m). If S_s is specified to be zero, the equation represents steady-state fluid flow.

2.1.2. Mechanical equilibrium equation

The equilibrium equation for stress is based on the observation that stress fronts travel much faster than fluid pressure fronts in the fluid or solid. Using tensorial notation, the mechanical equilibrium equation for the solid is expressed as

$$-\sigma_{ij,j} = F_i, \quad i, j = 1, 2, 3, \quad (2)$$

where σ_{ij} is the stress tensor (Pa) in the solid and F_i the component of the body force (N/m^3).

The constitutive equation defines the relation between the total bulk stress components (Pa), σ_{ij} and strain components, ε_{ij} when the effect of fluid pressure P is also included. The stress–strain law is given by

$$\sigma_{ij} = D_{ijkl} \varepsilon_{kl} - \alpha \delta_{ij} P, \quad i, j = 1, 2, 3, \quad (3)$$

where D_{ijkl} is the elasticity tensor (Pa), and is related to the Young's modulus E and Poisson's ratio ν for isotropic elastic media, which is degraded with damage initiation and development, α is Biot's effective stress coefficient (dimensionless), δ_{ij} is the Kronecker delta function, $\varepsilon_{ij} = (U_{i,j} + U_{j,i})/2$ and U_i represents the displacement vector of the solid. In this equation, the effect of fluid flow on the mechanical response of the solid skeleton is included by including the action of fluid pressure P via the effective stress in Eq. (3).

2.1.3. Evolution of damage variable and permeability

In the RFPA code, a damage mechanics-based constitutive law is proposed and incorporated into a finite element code for simulating the failure process in rock. In this code, when a crack is propagating within a finite element, an element is deemed to have partially failed, but is not removed from the computations. This treatment of crack propagation in isotropic media allows the evolution of fracture paths within individual elements and is able to accommodate crack growth in any arbitrary direction without the need for remeshing. The characteristics of the elements can be described with a constitutive law based on continuum damage mechanics [10].

As illustrated in Fig. 1, the damage constitutive relation for an element under uniaxial compressive and tensile stress is used to simulate the failure process. When the stress of the element satisfies the strength criterion (including the Coulomb criterion and maximum tensile stress criterion), the element begins to accumulate damage. In elastic damage mechanics, the elastic modulus of the element is degraded gradually as damage progresses, and the elastic modulus of the damaged element is defined

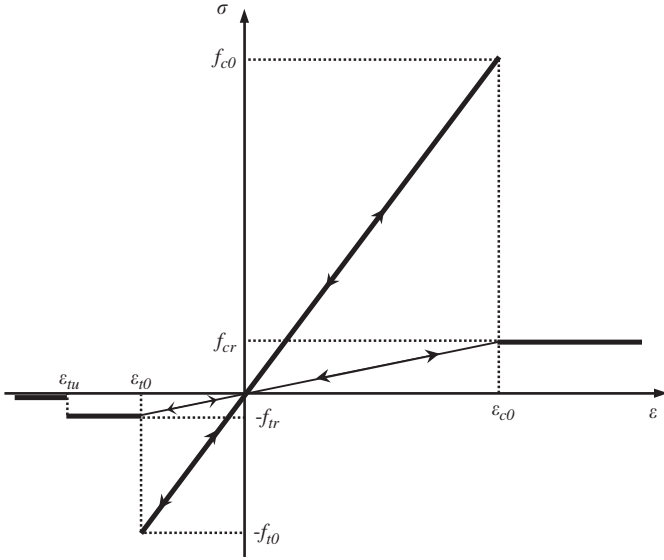


Fig. 1. Elastic damage constitutive law of element under uniaxial stress state. Here, f_{t0} and f_{tr} are uniaxial tensile strength and residual uniaxial tensile strength of the element, respectively; f_{c0} and f_{cr} are uniaxial compressive strength and residual strength of the element, respectively.

as follows:

$$E = (1 - \omega)E_0, \quad (4)$$

where ω represents the damage variable, and E and E_0 are the elastic moduli of the damaged and undamaged elements, respectively. The element and its damage are assumed to be isotropic, and so E , E_0 and ω are all scalar quantities. When $\omega = 1$, Eq. (4) predicts a zero value for the elastic modulus, which may lead to ill-conditioning in finite element calculations. To avoid this problem, the elastic modulus of a damaged element should not be allowed to fall below a very small value that was set to be 1.0×10^{-5} MPa in all numerical simulations of the present study. The damaged elastic moduli are used to calculate the elasticity tensor D_{ijkl} in Eq. (3).

When the tensile stress in an element reaches its uniaxial tensile strength, f_{t0} ,

$$\sigma_3 \leq -f_{t0}, \quad (5)$$

the damage variable ω of the element under uniaxial tension, as shown in the third quadrant of Fig. 1, can be expressed as

$$\omega = \begin{cases} 0 & \varepsilon > \varepsilon_{t0}, \\ 1 - \lambda \varepsilon_{t0} / \varepsilon & \varepsilon_{tu} < \varepsilon \leq \varepsilon_{t0}, \\ 1 & \varepsilon \leq \varepsilon_{tu}, \end{cases} \quad (6)$$

where λ is the residual strength coefficient, which is given as $f_{tr} = \lambda f_{t0}$. The uniaxial tensile strength of elements is considered to closely related to their uniaxial compressive strength via $f_{t0} = \kappa f_{c0}$, where κ is the ratio between uniaxial tensile and compressive strength of elements, and is specified as 0.1 in this study. The parameter ε_{t0} is the tensile strain at the elastic limit, and is called the threshold

strain, and ε_{tu} is the ultimate tensile strain of the element, describing the state at which the element would lose its load capacity for tension. The ultimate tensile strain is defined as $\varepsilon_{tu} = \eta \varepsilon_{t0}$, where η is called the ultimate strain coefficient.

Under multiaxial stress states the element still damages in tensile mode when the equivalent major tensile strain $\bar{\varepsilon}$ attains the above threshold strain ε_{t0} . The equivalent principal strain $\bar{\varepsilon}$ is defined as

$$\bar{\varepsilon} = -\sqrt{\langle -\varepsilon_1 \rangle^2 + \langle -\varepsilon_2 \rangle^2 + \langle -\varepsilon_3 \rangle^2}, \quad (7)$$

where ε_1 , ε_2 and ε_3 are three principal strains, and $\langle \cdot \rangle$ is a function defined as follows:

$$\langle x \rangle = \begin{cases} x & x \geq 0, \\ 0 & x < 0. \end{cases} \quad (8)$$

The constitutive law for an element subjected to multiaxial stresses can be easily obtained by replacing the strain ε in Eq. (6) with equivalent strain $\bar{\varepsilon}$. The damage variable is expressed as

$$\omega = \begin{cases} 0 & \bar{\varepsilon} > \varepsilon_{t0}, \\ 1 - \lambda \varepsilon_{t0} / \bar{\varepsilon} & \varepsilon_{tu} < \bar{\varepsilon} \leq \varepsilon_{t0}, \\ 1 & \bar{\varepsilon} \leq \varepsilon_{tu}. \end{cases} \quad (9)$$

To describe the element damage under a compressive or shear stress condition, the Mohr–Coulomb criterion is chosen as the second damage criterion, which is

$$\sigma_1 - \sigma_3 \frac{1 + \sin \phi}{1 - \sin \phi} \geq f_{c0}, \quad (10)$$

where σ_1 is the major principal stress, σ_3 is the minor principal stress, ϕ is the friction angle and f_{c0} is the uniaxial compressive strength. The damage variable under uniaxial compression is described as

$$\omega = \begin{cases} 0 & \varepsilon < \varepsilon_{c0}, \\ 1 - \lambda \varepsilon_{c0} / \varepsilon & \varepsilon \geq \varepsilon_{c0}, \end{cases} \quad (11)$$

where ε_{c0} is the compressive strain at the elastic limit, λ is a residual strength coefficient, and $f_{cr}/f_{c0} = f_{tr}/f_{t0} = \lambda$ is assumed to be true when the element is under uniaxial compression or tension.

When the element is under a multi-axial stress state and its strength satisfies the Mohr–Coulomb criterion, the maximum principal strain (maximum compressive principal strain) may be evaluated at the peak value of the maximum principal stress (maximum compressive principal stress) ε_{c0} .

$$\varepsilon_{c0} = \frac{1}{E_0} \left[f_{c0} + \frac{1 + \sin \phi}{1 - \sin \phi} \sigma_3 - \nu(\sigma_2 + \sigma_3) \right], \quad (12)$$

where ν is Poisson's ratio, σ_1 and σ_3 are major and minor principal stresses, respectively.

We assume that the shear damage evolution is only related to the maximum compressive principal strain ε_1 .

Correspondingly, we use the maximum compressive principal strain ε_1 of the damaged element to substitute for the uniaxial compressive strain ε in Eq. (11). Thus, Eq. (11) may be straightforwardly extended to triaxial stress states for shear damage as

$$\omega = \begin{cases} 0 & \varepsilon_1 < \varepsilon_{c0}, \\ 1 - \lambda \varepsilon_{c0} / \varepsilon_1 & \varepsilon_1 \geq \varepsilon_{c0}. \end{cases} \quad (13)$$

Experimental results indicate that permeability is strongly affected by stress level. This results both from the closure of pore walls, and from the generation of new pore volume. In the following, the variation of permeability is specified to be dependent on the stress and the accumulating damage to the rock. Zhu and Wong [24] concluded that for sandstone in the brittle field, for rocks with less than 15% porosity, permeability increased after the onset of dilatancy, whereas above 15% porosity the permeability constantly decreases, even when dilatancy (i.e., porosity increase) occurs. As early as 1975, Zoback and Byerlee [25] reported an increase of the permeability of granite when the granite sample became dilatant due to microfracturing. Brace [26] reported an increase of nearly threefold in the permeability of granite at high stress. Therefore, for the different rock and for the same rock with different porosity, the stress-dependent permeability evolution is actually different. In this study, we focused on a kind of granite, which is a crystalline rock similar to the one experimented by Zoback and Byerlee [25] and Brace [26], therefore, permeability enhancement after microfracturing is expected. During elastic deformation, rock permeability decreases as the rock compacts, and increases when the rock expands. However, the variation of permeability in these situations is limited in the pre-failure region. In the post-failure region, a dramatic increase in rock permeability can be expected as a result of the generation of numerous micro-fractures. The damage-dependent permeability can be defined as

$$k = \begin{cases} k_0 \exp[-\beta(\sigma_v - \alpha P)] & \omega = 0, \\ \xi k_0 \exp[-\beta(\sigma_v - \alpha P)] & 0 < \omega \leq 1, \end{cases} \quad (14)$$

where k_0 is the initial permeability, $\sigma_v = (\sigma_1 + \sigma_2 + \sigma_3)/3$, P the fluid pressure, β the coupling coefficient, and ξ the permeability scaling factor when damage occurs. When damage occurs, the local permeability in the damaged elements can change instantaneously from an initial value to a large value, ξ is used to reflect the increase in permeability.

The above formulations have been implemented into our self-developed numerical code rock failure process analysis (RFPA) [5,10,23]. Previous work with the code [5,10] has shown that, provided the residual strength coefficient λ and ultimate strain coefficient η are in the range $0 < \lambda \leq 0.1$ and $2 \leq \eta \leq 5$, respectively, the effect of constitutive parameters on failure evolution is minor. Therefore, when RFPA is used to study the brittle failure of rock, these two parameters must be specified within their respective ranges.

In the all simulations below in this study, $\lambda = 0.1$ and $\eta = 2.0$ are adopted. The code has been verified extensively and been used to investigate fracture initiation, propagation and breakdown behavior in permeable rocks. In this study, the RFPA is extended from a statistical realization-based simulation tool to a DIB tool.

2.2. Digital image processing technique

Digital images of rocks are obtained by photographing fresh cross-sections of rock samples with a digital camera, or by recovering a volumetric map of some proxy variable by using some non-destructive characterization methods. These include maps of density recovered by X-ray CT scanning, acoustic velocity or seismic imaging, or a variety of other geophysical indices. These digital images may be processed to enhance the recovery of the material microstructure. The pre-treatment includes image contrast enhancement and noise removal [20]. For a gray image, one integer value represents the gray intensity at each pixel. For true color (RGB; red, blue, green) images, there are three integer values to represent the red, green and blue level at each pixel. Therefore, the color image data consist of three discrete functions, $f_k(i, j)$, where $k = 1, 2$ or 3 , in the i and j Cartesian coordinate system:

$$f_k(i, j) = \begin{bmatrix} f(1, 1) & f(1, 2) & \cdots & f(1, M) \\ f(2, 1) & f(2, 2) & \cdots & f(2, M) \\ \vdots & \vdots & & \vdots \\ f(N, 1) & f(N, 2) & \cdots & f(N, M) \end{bmatrix} \quad (k = 1, 2, \text{ and } 3 \text{ for RGB image}), \quad (15)$$

where i varies from 1 to N , and j from 1 to M , and M and N are the number of pixels in the horizontal and vertical directions, respectively. For gray images, only a single variable ($k = 1$) is necessary.

In this work the discrete function, $f_k(i, j)$ of a digital image of JPEG or Bitmap format is utilized (this is recovered via a macro-routine programmed in MATLAB). As an alternative to the RGB color space, the hue, saturation, intensity (HSI) color space may be used, as it is close to how humans perceive colors [27]. The hue component (H) represents repression related to the dominant wavelength of the color stimulus. Therefore, the hue is the domain color perceived by human beings. The saturation component (S) represents how strongly the color is polluted with white. The intensity component (I) stands for brightness or lightness and is irrelevant to colors. In general, hue, saturation, and intensity are obtained by different transformation formulae by converting numerical values of R , G , and B in the RGB color space to the HSI color space. The values of S and I vary from zero to one. But the value of H varies from 0 to 360, which can also be normalized to be from 0 to 1.

Distinct microstructures (such as fractures and minerals) with different perceived colors in the rock sample are acquired according to the values of H , S , or I of individual pixels, and the different material properties (such as Young's modulus and permeability) are specified for each pixel according to its catalog of minerals or colors. In theory, the material properties of different minerals or structures must be known based on mineralogical analysis of the rock sample, by this means, the relation between values of I (H or S) of the digital image pixels and their materials properties can be uniquely established. Since this study is to tentatively illustrate the capability of DIB technique and the effect of heterogeneity on hydromechanics, the parameters such as Young's modulus and permeability are only specified based on artificial specification of reasonable values. Anyway, heterogeneity characterization based on DIB techniques provides a novel method that permits the particular effect of rock microstructures and heterogeneity on the hydromechanical process to be clearly isolated and studied.

2.3. Digital-image-based (DIB) simulation

In DIB simulations, an image of a rock sample is discretized into many square elements of identical size, and these elements map directly onto finite elements used for stress analysis. The material parameters for each pixel are specified for the corresponding finite element. When the Young's moduli and permeability of these minerals are defined for an individual element, the distributions of Young's modulus and permeability throughout the medium is also specified. Using this technique, the basic governing equations are the same for all components (i.e., minerals), but the material properties may differ.

During simulation, the model is loaded in a quasi-static fashion. At each loading increment, the fluid flow and stress equations in the elements are solved and a coupled analysis is performed. The stress state of each element is checked at each calculation step. Tensile or shear damage occurs when the stress or strain state of elements meets the maximum tensile stress criterion or the Mohr–Coulomb criterion in compression, respectively. At a given deformation/loading level, the tensile damage threshold is always checked first and if found to be attained, then a check of the Mohr–Coulomb threshold is omitted; the Mohr–Coulomb threshold is checked only when the tensile threshold is not attained. Damage applied to overstressed elements leads to the reduction of stiffness and strength, and an increase in permeability. In this respect, totally damaged elements ($\omega = 1.0$) are considered as microcracks. Macroscopic cracks may form where these microcracks propagate and coalesce. Subsequently, the next load increment is added only when there are no more elements strained beyond the strength threshold level at an equilibrium strain field.

3. Verification

The code RFPA has been verified comprehensively and been used to investigate fracture initiation, propagation and breakdown behavior in permeable rocks [5–7,10]. The numerical simulations of hydromechanical problems by RFPA have also been presented elsewhere [5,23]. Therefore, the verification in this study is mainly focused on the DIB technique. Two verification examples are conducted to examine the capability of DIB technique and its implementation into RFPA. In the first example, we used an artificial image of rock including a pre-existing crack with an inclination angle of 45° . The digital image was incorporated directly into the finite element simulation. The simulated wing crack propagation patterns are compared with previous experimental observations. In the second verification example, a Weibull distribution is used to generate material property maps. These statistically generated images are then incorporated directly into the finite element simulation. In this case, the exact relations between the color index and material properties are known. This example was used to determine the impact of digital image processing on simulation accuracy. The results are reported in the following sections.

3.1. Wing crack propagation

Fig. 2(a) presents the artificial digital image of a fractured rock with a pre-existing crack (the inclination angle is 45°). The dimension of the simulation domain is $100\text{ mm} \times 200\text{ mm}$, and the length of the pre-existing crack is $30\sqrt{2}\text{ mm}$. We assume that the fracture is not open, but filled with a weak material. A low magnitude of the Young's modulus ($1.0 \times 10^{-8}\text{ MPa}$) is specified to the infilling material in the fracture. The fracture is pre-existing, and will not be damaged again, and therefore a relatively high strength of 900 MPa is specified. In this case, only two distinct materials are present in the domain, and these are the fracture and matrix. We use the color index as a criterion to specify the material properties as shown in Table 1. The internal frictional angle and ratio of compressive and tensile strength are fixed to be 30° and 10, respectively, for both fracture and matrix. As illustrated in Fig. 2(b), a displacement of 0.002 mm is applied step by step in the vertical direction, whilst a zero vertical displacement is imposed at the base.

Fig. 3 presents the load–displacement curve (Fig. 3(a)), the simulated cracking patterns (Fig. 3(b)) and the experimental observations (Fig. 3(c)). The simulated cracking patterns compare well with experimental observations. The fracturing starts at the tips of the fracture and propagates in a curvilinear path as the load increases. Wing cracks are tensile cracks, and they grow in a stable manner, since an increase in load is necessary. Therefore, during the propagation of wing cracks, the load–displacement curve remains linear until the peak load. Wing cracks tend to align with the direction of the applied uniaxial compressive

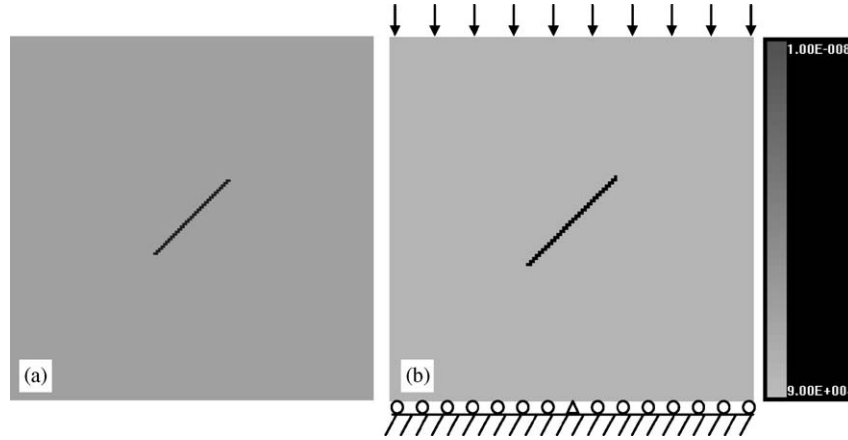


Fig. 2. The artificial rock image as well as the quantified Young's modulus map based on DIB technique: (a) rock image; (b) Young's modulus map.

Table 1
Young's modulus and strength of artificial fractured rock

Values of I	Material	Young's modulus (MPa)	Uniaxial compressive strength (MPa)
$0.0 \leq I < 0.01$	Filled material in fracture	$1.0e-08$	900.0
$0.01 \leq I \leq 1.0$	Rock matrix	90,000.0	200.0

stress. After the peak load is reached, secondary cracks initiate from the tips of the fracture, which leads to the sudden loss of load capacity of the rock sample. These numerical results agree well with experimental observations [28].

3.2. Comparison with statistical-based simulation

As in previous numerical simulations of RFPA, we assign rock heterogeneity based on a statistical distribution [5–7,10,23]. In those simulations, the rock is assumed to be composed of many mesoscopic elements of identical size, with the mechanical properties of elements assumed to conform to a given Weibull distribution as defined in the following probability density function (pdf):

$$f(u) = \frac{m}{u_0} \left(\frac{u}{u_0}\right)^{m-1} \exp\left[-\left(\frac{u}{u_0}\right)^m\right], \quad (16)$$

where u is the mechanical parameter of the element (such as strength or elastic modulus); the scale parameter u_0 is related to the average of the element parameters and the parameter m defines the shape of the distribution function. From the properties of the Weibull distribution, a larger value of m implies a more heterogeneous material and vice versa. Therefore, the parameter m is called the homogeneity index in these numerical simulations. Using the pdf

in a computer simulation of a medium composed of many mesoscopic elements, one can produce a heterogeneous material numerically.

Fig. 4 shows a numerical specimen which is produced based on a Weibull distribution with a homogeneous index of $m = 3.0$, with the histogram of Young's modulus also shown. This numerical specimen is composed of 40,000 elements. The gray scale in this Fig. 4(a) denotes the relative magnitude of Young's modulus. Fig. 4(b) shows the distribution of Young's moduli of the elements, whose maximum and minimum values are 114,000 and 6000 MPa, respectively.

In this verification example, we conducted two parallel simulations. The first one is the statistically based simulation using the RFPA code, in which the material heterogeneity is specified directly according to Eq. (16). The second is the DIB simulation, in which the material heterogeneity is characterized and quantified based on the image of Young's modulus produced by RFPA during the first simulation. If high accuracy of DIB technique is achieved, two numerical simulations will give the same results. This verification includes the following steps.

Firstly, the statistically generated material properties (for example, Young's modulus) were incorporated directly into the finite element simulation. The failure process of this numerical specimen (Fig. 4(a)) was simulated. Secondly, using RFPA, we used the following gray scale to create the material property images of Young's modulus:

$$G_d = \frac{E - E_{MIN}}{E_{MAX} - E_{MIN}}, \quad (17)$$

where G_d is the gray scale [0,1], E the Young's modulus of any element, and E_{MAX} and E_{MIN} the maximum and minimum values of Young's modulus of all the elements. The resulting image is shown in Fig. 4(a).

Thirdly, we setup another numerical specimen with RFPA, using the digital image processing technique to read the material property image and to assign the Young's

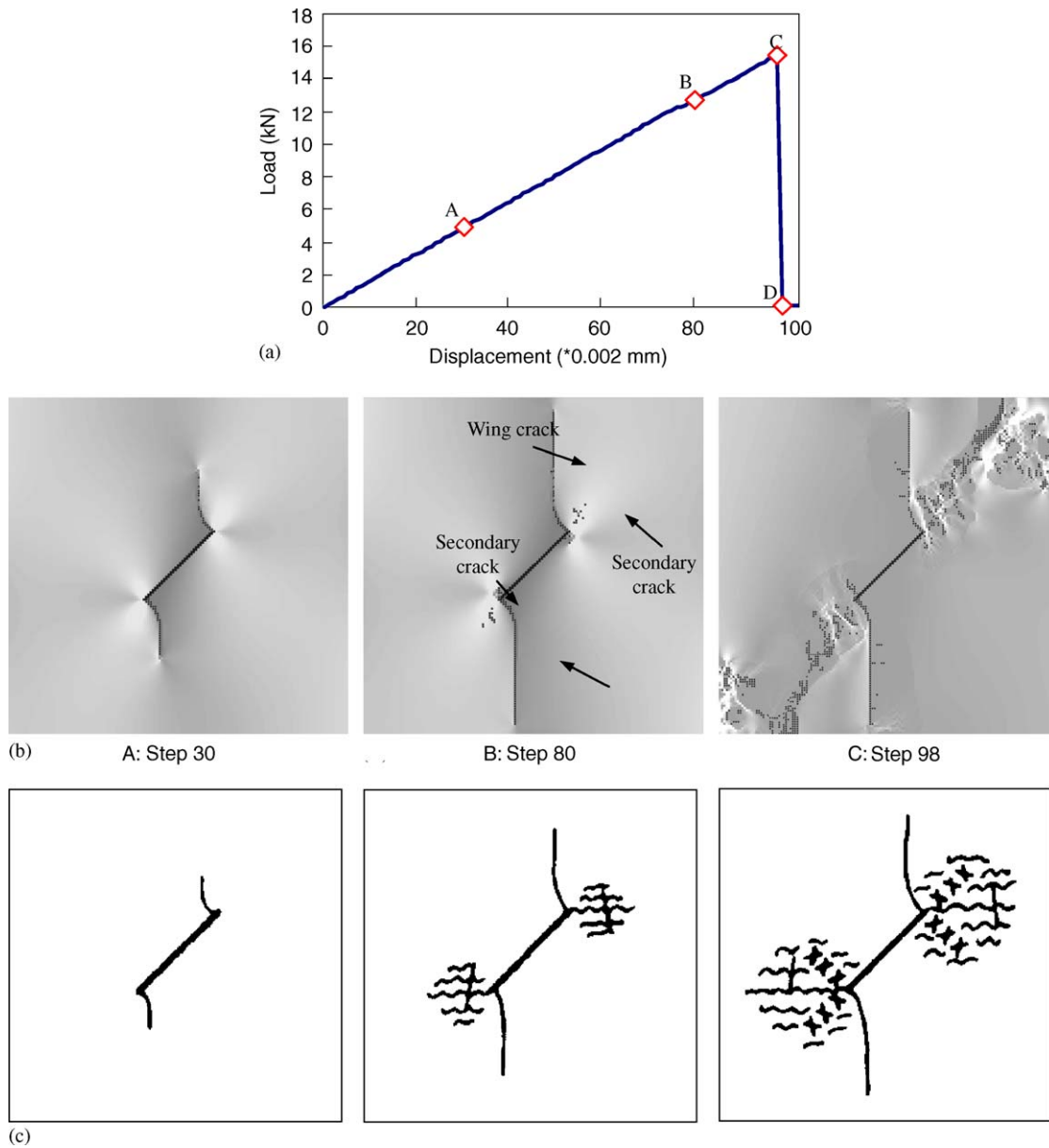


Fig. 3. The load–displacement curve and cracking patterns of the rock sample with a pre-existing crack: (a) load–displacement curve (numerical results); (b) failure patterns (numerical results); (c) cracking patterns (experimental results after Lajtai (1974)).

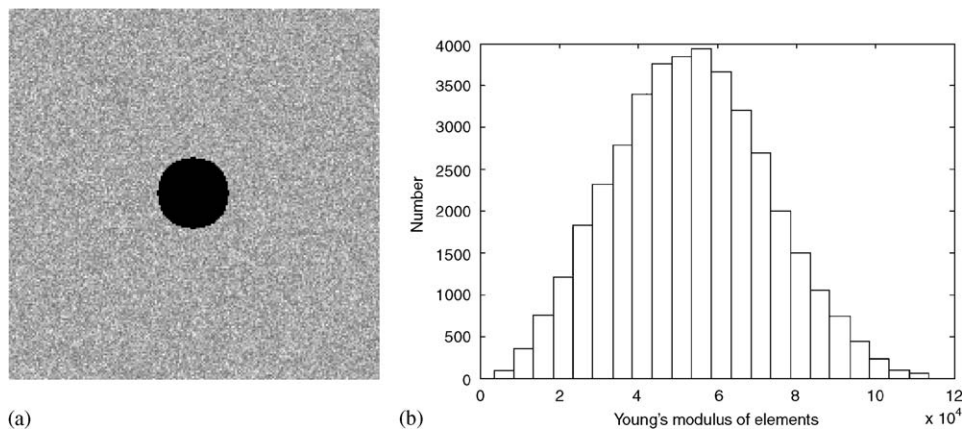


Fig. 4. The statistically generated numerical specimen. The material properties of elements in the numerical specimen conform to the Weibull distribution with homogeneity index of $m = 3.0$: (a) numerical specimen; (b) histogram of material properties of elements.

modulus based on the following equation:

$$E = E_{\text{MIN}} + (E_{\text{MAX}} - E_{\text{MIN}})G_d. \quad (18)$$

We applied a similar procedure to define the material strengths.

In theory, the material properties should be completely identical because we knew exactly the relations between the gray scale and the material properties (as expressed by Eqs. (18) and (19)). Therefore, any discrepancies between two simulations would have to come from the digital image processing technique.

In these two simulations (statistical based simulation and DIB simulation), the same specimen size and boundary condition are specified. The numerical specimens are subjected to uniaxial compression in the vertical direction. A vertical displacement of 0.002 mm is applied step by step, while a zero vertical displacement is applied at the base. Fig. 5(a) presents the curve between Young's moduli given according to the statistical generation and those quantified by using

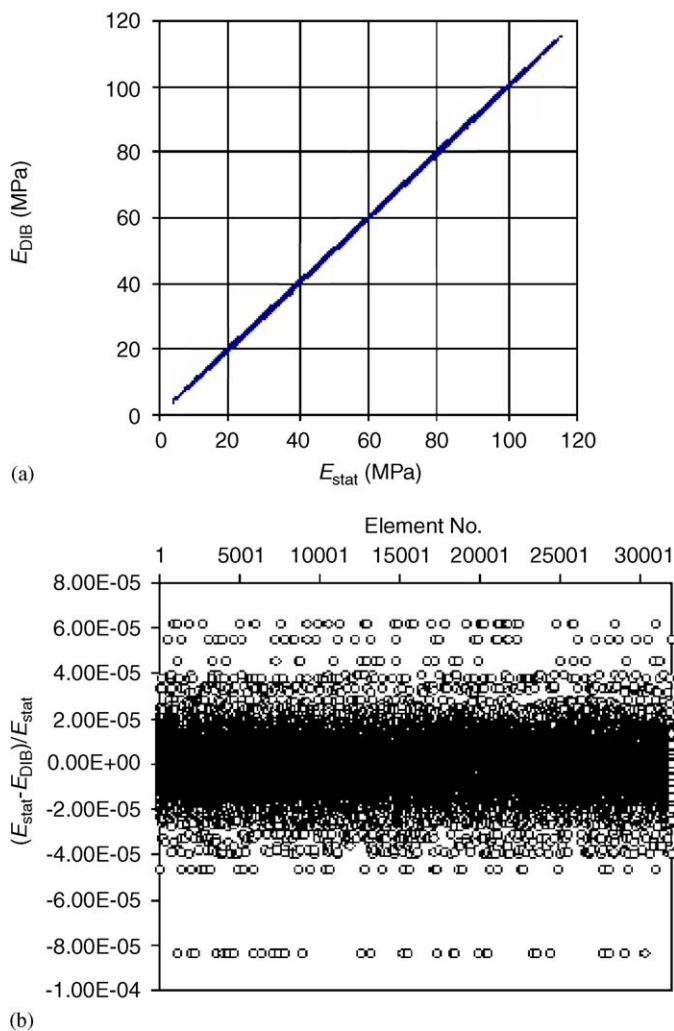


Fig. 5. Comparison of the Young's moduli specified according to the Weibull distribution (E_{stat}) and those (E_{DIB}) defined by the DIB technique: (a) the correlation between E_{stat} and E_{DIB} ; (b) relative errors between E_{stat} and E_{DIB} .

the DIB technique. It can be seen that their correlation is small with a largest relative error of only 0.008%.

Fig. 6 shows the failure process of numerical specimens when simulated based on the statistical generation and the DIB technique, respectively. It is found that the failure patterns at each strain level are almost identical to each other, although there are some small local differences for the crack propagation path. This also means that the failure patterns are very sensitive to the local heterogeneity of rock, which determines where the crack initiation occurs, and sometimes the small distinctions in some locations can lead to a quite different crack propagation path and the final failure pattern.

4. Effects of heterogeneities on hydromechanics

In DIB simulations, digital images are incorporated directly into the DIB micro-hydromechanics model. Image voxels are mapped directly to equivalent mechanical and flow properties as defined by the voxel color. These property maps are ported to the model and are capable of solving directly for the evolving deformation, and fluid velocity fields. In this section, we apply this DIB simulation approach to a 2D case to investigate the hydromechanics of a fractured rock sample under applied uniaxial compression. The following 4 steps show how the DIB finite element simulation technique works:

Step I: A digital image of the fractured rock with high resolution is taken by a digital camera, and its HSI values are obtained and analyzed.

Step II: A two-dimensional DIB model is developed, in which Young's modulus, strength and permeability are chosen as heterogeneous input parameters.

Step III: Different boundary conditions are applied to the rock sample in order to study their effect on the rock failure process and associated flow characteristics.

Step IV: Simulation results are presented through graphical animations.

4.1. Digital image of rock sample and its processing

Fig. 7(a) presents the digital image of a rock sample (granite from King's Park, Perth, Western Australia). The size of the rock sample is 200 mm × 200 mm, and the resolution of the image is 200 × 200 pixels. That is to say, the size of a pixel is 1 mm. In order to capture the heterogeneous details of rock surface as accurate as possible, the higher resolution of the digital image is necessary. The size of finite elements must be small than the size that a pixel represents, in order to avoid losing the heterogeneous information that the pixel contains. In routine application, we are not intending to simulate the microscopic details of the rock, and therefore much too fine digital image is not necessary. The exposed face provides a cross section that includes several distinct macroscopic fractures. Fig. 7(b)–(d) presents the distributions of the values of H , S and I , for the image. Through

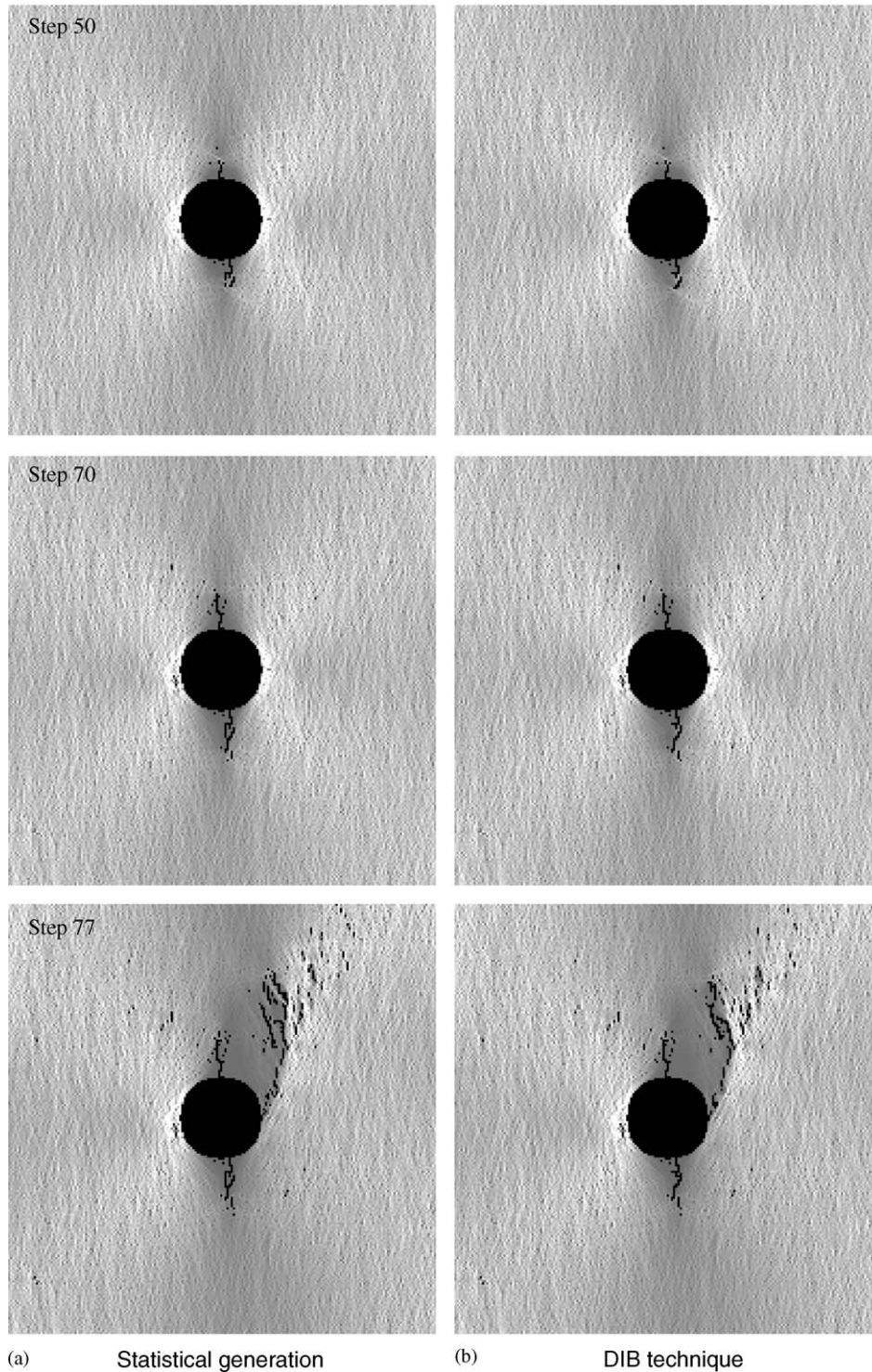


Fig. 6. Comparison of failure patterns that are simulated using statistical generation and the DIB technique. The applied displacement in vertical direction is 0.002 mm/step: (a) statistical generation; (b) DIB technique.

comparisons, we conclude that the distribution of I values can capture the most important heterogeneous features such as fractures in the rock sample. Of course, the identification of minerals is depended on the resolution of the image, in order to exactly distinct the minerals with their I values should be based on professional mineral analysis.

4.2. Rock heterogeneity characterization and quantification

In theory, the identification of minerals in the rock must be based on mineral analysis using microscopy. Because this is only a tentative study that illustrates the feasibility of digital image technique to characterize and to quantify the rock heterogeneity, the relation between hydromechanical

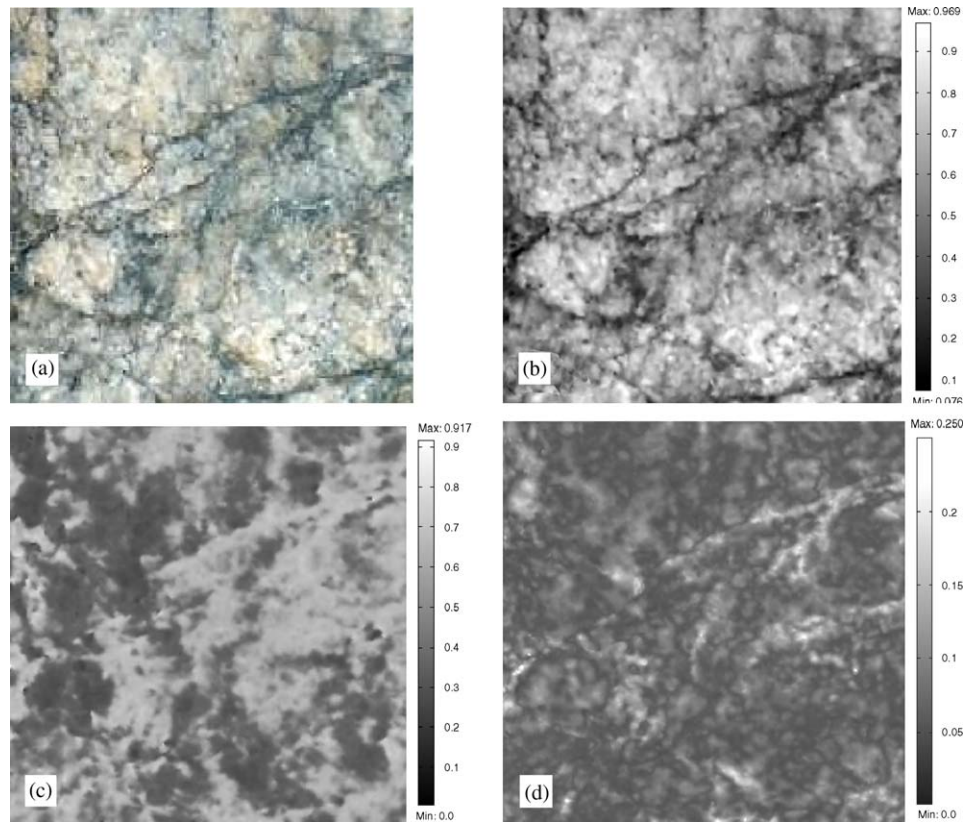


Fig. 7. The digital image of section of the rock sample cross-section, and its HSI values of pixels: (a) digital image of rock sample; (b) I values of pixels; (c) H values of pixels; (d) S values of pixels.

properties of rock and the I values of DIB on mineral analysis and related experiments is needed for further study in near future.

In this tentative study, we characterize the rock heterogeneity at two hierarchical levels. For the first level, we set two different thresholds to distinguish rock fractures and matrixes, respectively. For the second level, we distinguish the rock fractures further into two sub-levels without mineral analysis, namely M1 and M2, and the rock matrixes further into three sub-levels, namely M3, M4 and M5, respectively. We assume that fractures are not open, but filled with two minerals, which are M1 and M2. This two-level scheme can represent the heterogeneities both in fractures and rock matrix in fine details, as shown in Fig. 8.

Thresholds of the values of I for these five components are artificially chosen and listed in Table 2. Correspondingly, the Young's modulus, strength and permeability maps are shown in Fig. 9. In a qualitative sense, lower magnitudes of the Young's modulus and the strength and higher magnitudes of permeability are assigned to the fracture components, M1 and M2.

4.3. Simulation models

In order to investigate the influence of local rock heterogeneities on the hydromechanical responses, simulations were conducted under four different loading conditions, namely, BC-I, BC-II, BC-III, and BC-IV,

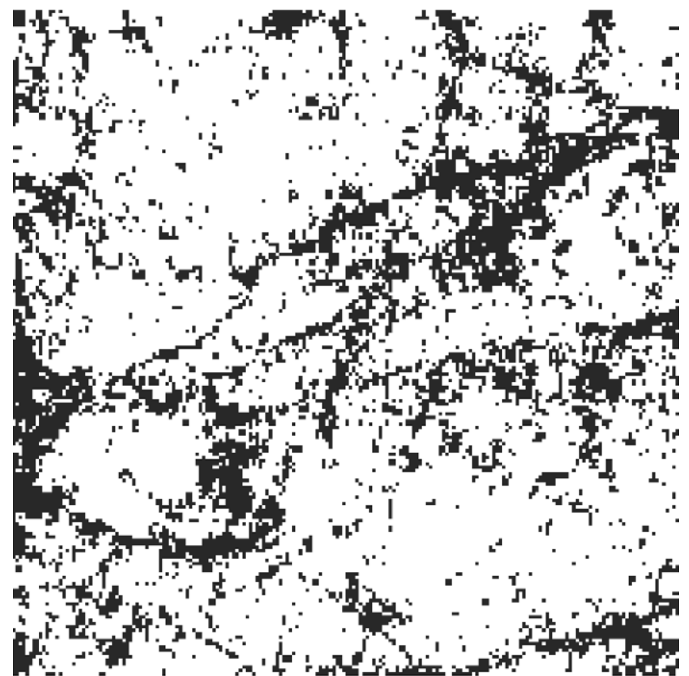


Fig. 8. The fractures distributed in the heterogeneous rock (here the black color denotes the fractures, while white color denotes rock matrix).

respectively. They are illustrated in Figs. 10(a)–(d). The rock sample is simulated as a plane stress problem. For the case of BC-I, the applied external displacement (d_e) of

0.004 mm is applied step by step in the vertical direction. Similar settings are applied for the case of BC-II. For the case of BC-III, a vertical displacement (d_c) of 0.004 mm is applied step by step under constant confining pressure until the rock loses its load-bearing capacity completely, while Dirichlet boundary conditions of constant fluid pressures $P_h = 7.5$ MPa and $P_l = 6.0$ MPa are applied on the upper and lower boundaries, respectively, while no flow conditions are imposed on the lateral boundaries. For the case of BC-IV, the axial loading and pressure gradient are applied in the horizontal direction, while the confining stress is applied in the vertical direction. With regard to the Biot's effective stress pressure coefficient α , as discussed by Al-Wardy and Zimmerman [29], the effective stress coefficient for the permeability is not a constant, but is sensitive to the pore structure, clay content, pore pressure and so on. During the failure process of rock, the pore structure of rock varies with time, and so is not a constant. However, because it is very difficult to obtain this parameter when all these factors are considered, for simplification, in this manuscript, the effective stress coefficient is assumed to be 0.9, and it is the same as for the macroscopic stress–strain curve. Other material parameters, such as the coupling coefficient β , the permeability index ξ and other material fitting parameters, which are selected based on previous simulations of RFPa [23], are also listed in Table 3.

Table 2
Young's modulus and hydraulic conductivity of minerals in the heterogeneous rock

Values of I	Minerals	Young's modulus (GPa)	Uniaxial compressive strength (MPa)	Permeability (m^2)
$0.0 \leq I < 0.2$	M1	8.0	20.0	$1.0e-14$
$0.2 \leq I < 0.4$	M2	30.0	100.0	$1.0e-15$
$0.4 \leq I < 0.6$	M3	80.0	150.0	$1.0e-16$
$0.6 \leq I < 0.8$	M4	70.0	250.0	$1.0e-16$
$0.8 \leq I \leq 1.0$	M5	90.0	150.0	$1.0e-16$

4.4. Simulation results

In the following, we use grayscale figures to show the magnitude of a parameter, where the intensity of the gray scale indicates the relative magnitude of the parameter. In our simulation results, damage of elements causes degradation of their elastic modulus and the completely damaged ones are displayed as black. Therefore, the figure of Young's modulus is useful to show the failure patterns as damage is accumulated. Similarly, in the maximum shear stress figures the brightness indicates the magnitude of maximum shear stress. In addition, in the figure of damage elements, all the damaged elements are denoted by different shades, i.e., white and dark gray for shear- and tension-damaged elements at the current step, respectively, and black for elements damaged in all the preceding steps.

4.4.1. Case BC-I: vertical loading

Fig. 11 shows the stress–strain curve as well as the evolution in the number of damaged elements with strain, for the sample under vertical compression. The stress–strain curve has a shape similar to that observed in many physical experiments. The Young's modulus and uniaxial compressive strength of this numerical specimen are 53.5 GPa and 38.2 MPa, respectively. It can be seen clearly that some elements are damaged under approximately 60% of the maximum load, but these damaged elements release little elastic strain energy. The stress–strain curve stays nearly linear up to the maximum load. Beyond the peak load, the load-bearing capacity drops rapidly, followed by a small residual strength.

Because the rock is inhomogeneous, the stress state in the numerical specimen varies from point to point. The shear and tensile stresses around the fractures maybe enhanced or diminished, depending on the orientation, geometry and stiffness of the fractures. The failure processes of the numerical specimen at 6 strain levels (as indicated by A–F in Fig. 11) are shown in Fig. 12. Initially, the damaged elements are distributed mostly in the

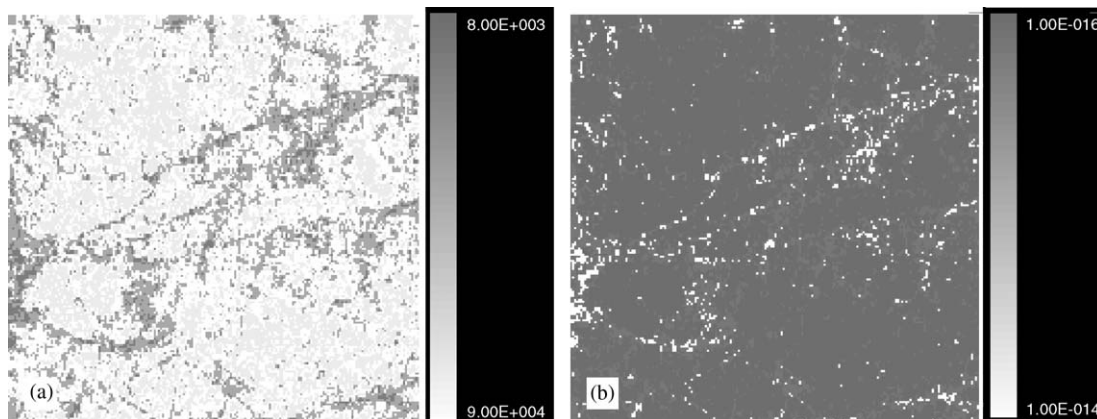


Fig. 9. Distribution of Young's modulus and permeability in this rock sample, defined using DIB technique: (a) Young's modulus map; (b) permeability map.

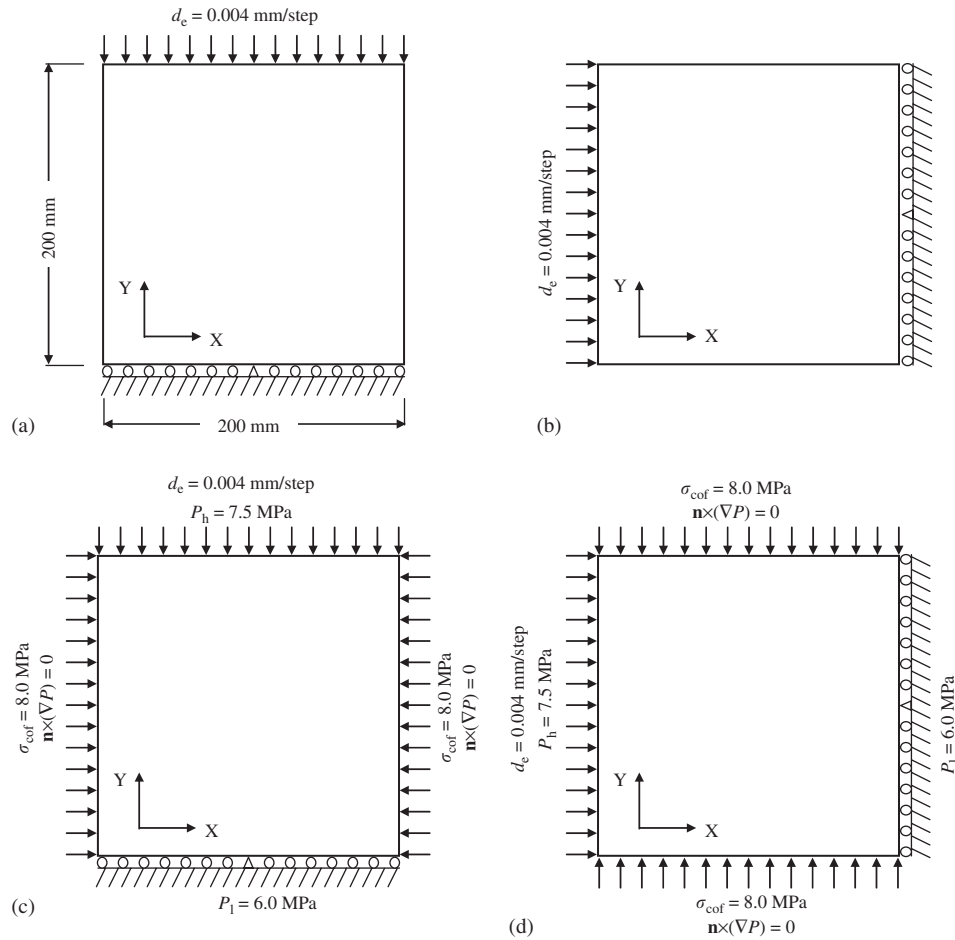


Fig. 10. Four cases of boundary conditions applied on the rock sample: (a) BC-I, uniaxial compression in vertical direction; (b) BC-II, uniaxial compression in horizontal direction; (c) BC-III, axially loaded and pressure gradient in vertical direction and with confining pressure in horizontal direction; (d) BC-IV, axially loaded and pressure gradient in horizontal direction and with confining stress in vertical direction.

Table 3
Material parameters used for the analysis of hydromechanical processes

Parameters	Value
Gravity acceleration, g (m/s ²)	9.8
Specific storativity, S_s (1/m)	0.0
Biot's effective stress coefficient, α (dimensionless)	0.9
Coupling coefficient, β (dimensionless)	0.02
Internal frictional angle, ϕ (deg)	30°
Poisson's ratio, ν (dimensionless)	0.25
Permeability increase factor, ξ (dimensionless)	500
Liquid dynamic viscosity, μ_1 (kg/m s)	1.0×10^{-3}
Density of fluid, ρ_1 (kg/m ³)	1.0×10^3

fractures. These damaged elements subsequently induce stress concentrations around them, causing tensile damage in the adjacent elements. At higher stress levels, adjacent damaged elements merge. At the first strain level after the peak load (point C: $\epsilon_a = 0.00071$), a large number of elements are damaged in tensile mode. This causes the initiation of cracks parallel to the loading direction, leading

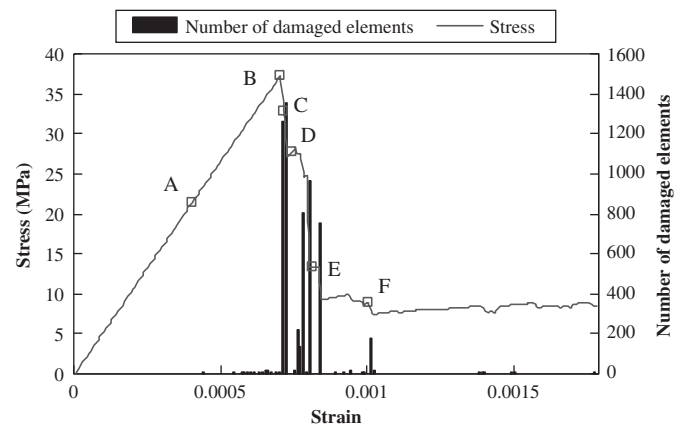


Fig. 11. The stress–strain curve as well as the number of damaged elements of the rock sample under uniaxial compression in vertical direction (BC-I).

to a sharp decrease in the load-bearing capacity of the sample. As the applied vertical displacement increases, more elements are damaged in tension, especially at the

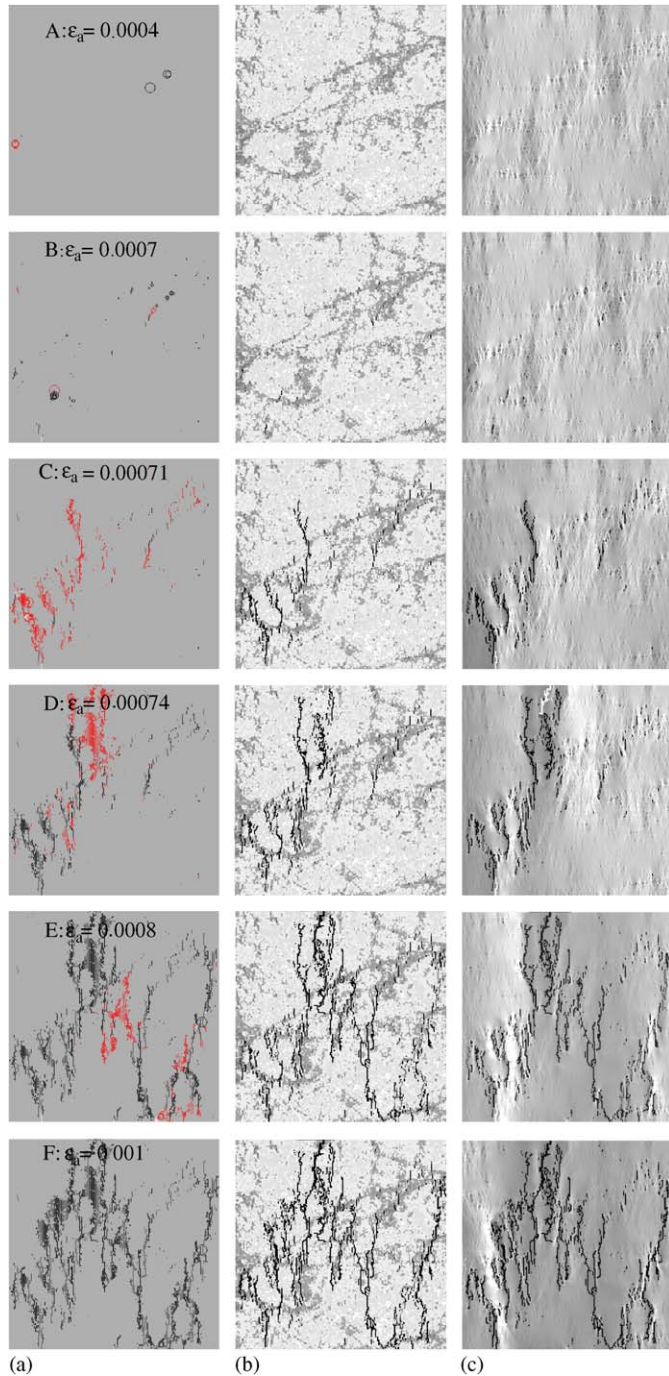


Fig. 12. The failure process of rock sample under uniaxial compression in vertical direction (BC-II); ε_a is the strain in the loading direction: (a) damaged elements; (b) Young's modulus; (c) maximum shear stress.

bridge between the cracks that previously formed in the fractures (for example, point E: $\varepsilon_a = 0.0008$). This leads to the propagation of macroscopic cracks parallel to the loading direction. The fractures have a significant effect on the initiation of cracks in the rock sample; however the macroscopic cracks that contribute to the instable failure do not solely propagate in the fractures, but also penetrate into the rock matrix. In this regard, we can come to the

similar conclusion as previously pointed by many researchers [30–32]: “under compression, a macroscopic crack can not develop from a single, pre-existing crack, but must be a result of the coalescence of crack branches and grain boundaries.”

4.4.2. Case BC-II: horizontal loading

When the sample is loaded under horizontal (uniaxial) compression, the stress–strain curve as well as the number of damaged elements is shown in Fig. 13. The Young's modulus and strength under this loading condition are 56.5 GPa and 30.9 MPa, respectively. The failure patterns are also shown in Fig. 13(b). Under this loading condition, the crack propagation path is more closely coincident with the distribution of fractures, where most of the damage is found. This is because the fractures in the rock sample are roughly distributed in the horizontal direction. The main macroscopic cracks are nearly parallel to the loading direction (horizontal direction).

The main macroscopic cracks are always nearly parallel to the loading direction no matter how the local heterogeneity affects the initiation of local damage. The numerical results of above two cases of boundary conditions indicate that the main macroscopic cracks that contribute to the instable failure of rock are locally controlled by the local heterogeneity of rock, but its final pattern is dominated by the loading directions.

4.4.3. Case BC-III: vertical loading and flow

Fig. 14 presents the permeability variation during the complete failure process of rock for Case BC-III. The overall permeability of the rock sample is obtained from the numerical sample as the ratio of volumetric flow rate per unit area to pressure gradient as

$$k = \frac{LQ}{P_h - P_l} \frac{\mu_l}{\rho_l g}, \quad (19)$$

where L is the length of the sample (200 mm), and Q the total flux flowing through the rock sample in the direction of pressure gradient. At the initiation of the test, the overall permeability of this heterogeneous rock sample, without stress, is calculated as $5.4 \times 10^{-15} \text{ m}^2$.

The damage of elements leads the variation of Young's modulus and permeability. Because of the local variation in permeability, the distribution of flow velocity is also modified. Fig. 15 shows the variation of Young's modulus (failure pattern), permeability, and flow velocity at different stages of loading, corresponding to strain levels as denoted A through D in Fig. 14.

In the pre-peak region of the stress–strain curve, the permeability decreases with the axial stress due to compaction. In this region, although some microcracks initiate in fractures, they do not coalesce to form a continuous flow channel (Fig. 15A), therefore the overall permeability decreases monotonically (Fig. 14). Because of the high permeability in the fractures, preferential flow in these fractures is observed, as shown in Fig. 15A.

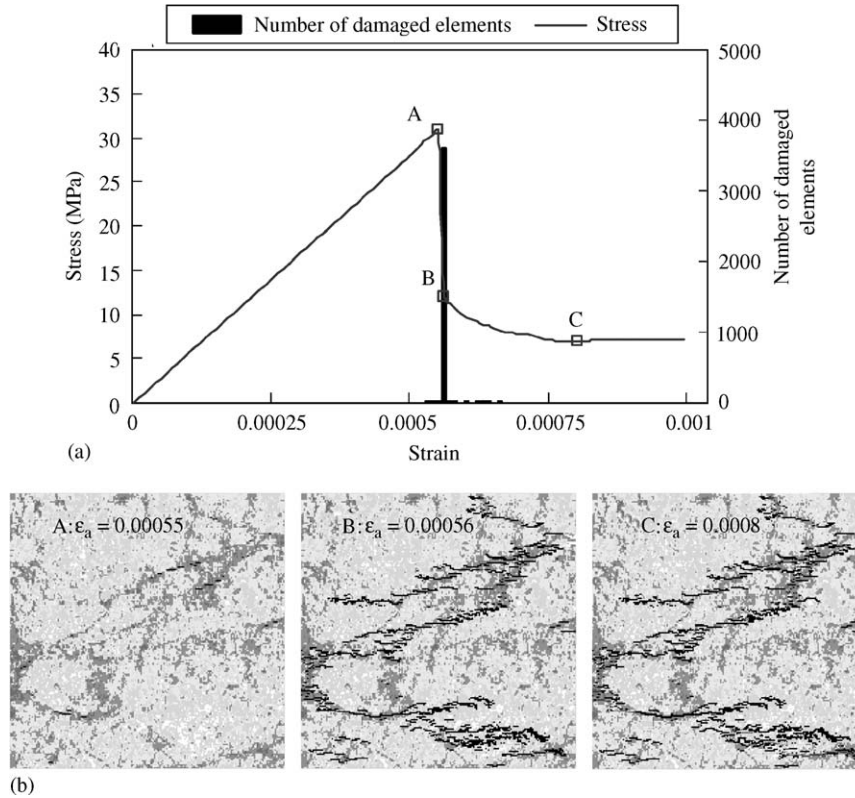


Fig. 13. Stress–strain curve of the rock sample under uniaxial compression in horizontal direction (BC-II): ϵ_a is the strain in loading direction: (a) the stress–strain curve as well as the number of damaged elements; (b) failure patterns (Young’s modulus) at strain levels A, B and C as denoted in (a).

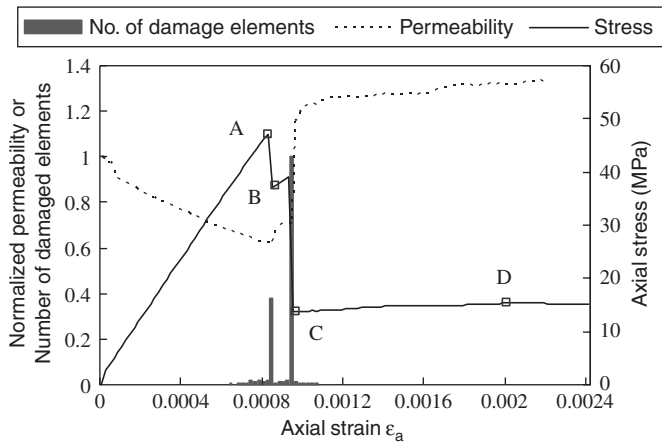


Fig. 14. The relationship among permeability, axial stress, number of damaged elements and axial strain under boundary condition BC-III. The magnitude of permeability is normalized to its initial values of $5.4 \times 10^{-15} \text{ m}^2$, while the number of damage elements is also normalized to its maximum value of 2927.

At a critical damage density, the stress peaks, and immediately post-peak cracks rapidly initiate in the fractures (Fig. 15B), which in turn lead to instable localized failure in the rock sample—permeability increases dramatically in this area. With an increase of the externally applied displacement, cracks propagate both upwards and

downwards to the top and bottom boundaries, where that flow is facilitated by preferentially connected fracture patterns.

In the post-peak region of the stress–strain curve, damage evolves to other groups of elements (Fig. 15C), which leads to the continuous increase in permeability and decrease in load-carrying capacity. In general, from the stress–strain curve, it can be seen that the rock sample gradually loses its load-carrying capacity, and no flow-through channel from top to bottom boundaries is formed. The overall permeability increase is to 1.25 times of its initial value.

As being found by other researcher [33], the permeability enhancement induced by local damage can dramatically alter the flux distribution (Fig. 15C). It is evident that the fracture patterns resulting from mechanical localization influence the large-scale transport properties.

4.4.4. Case BC-IV: horizontal loading and flow

Under boundary conditions BC-IV, the variation in permeability with loading is shown in Fig. 16. In contrast to the numerical results in Fig. 14, the confined compressive strength varies from 47.1 MPa in Case BC-III to 51.9 MPa in Case BC-IV. Under this boundary condition, the permeability decreases to 62% of its initial value at peak stress, and increases to 133% of its initial value in the

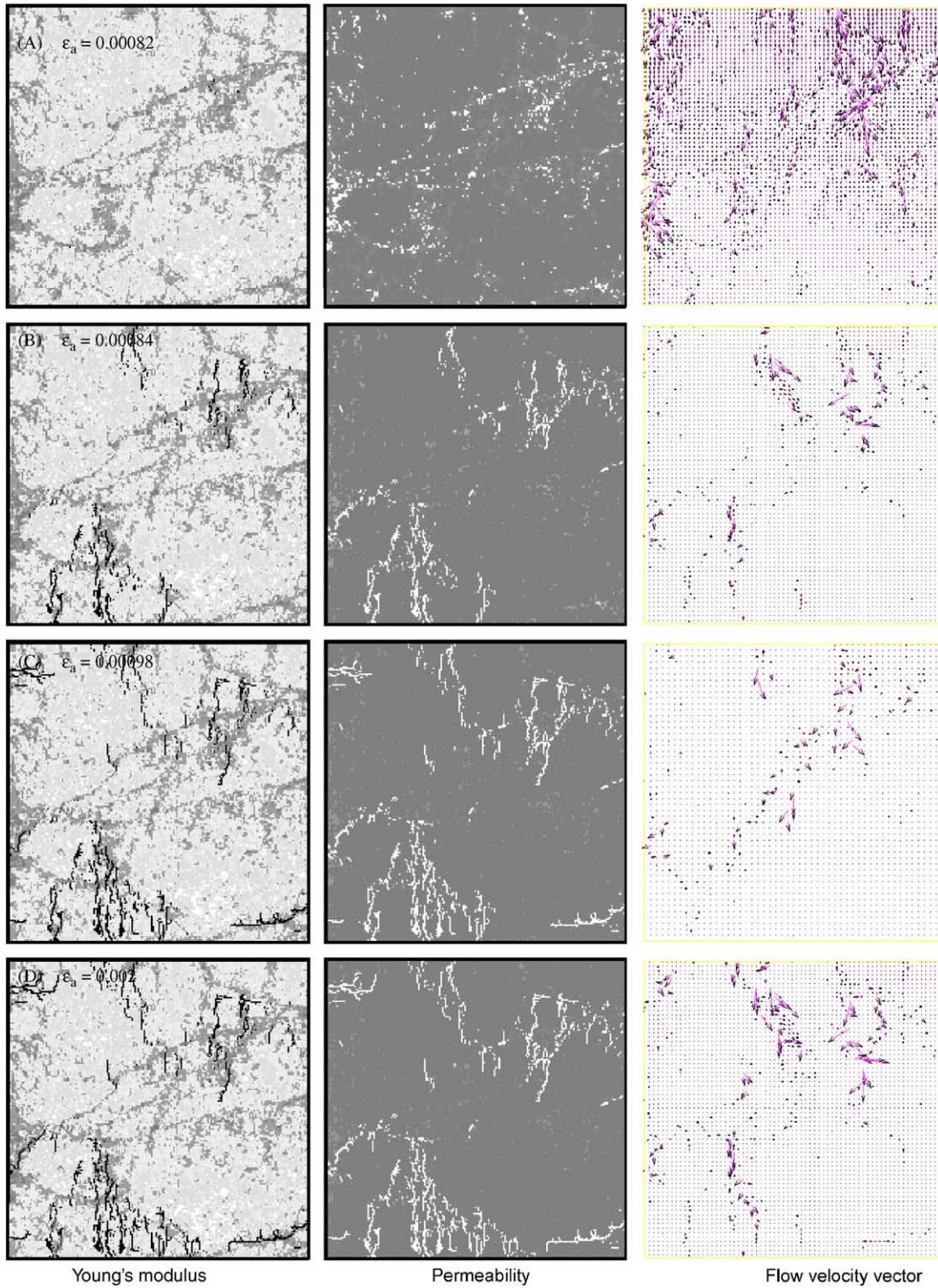


Fig. 15. The variation of Young's modulus, permeability and flow vector of rock sample under boundary condition BC-III. The confining stress is 8.0 MPa, the hydraulic pressures at the top and bottom boundaries are 7.5 and 6.0 MPa, respectively, and ϵ_a is the axial strain in vertical direction.

final state. Except for these specific changes in critical values of strength and permeability, the stress versus strain and permeability versus strain curves show the same tendency as that in Fig. 14.

Fig. 17 presents the evolution of the Young's modulus, permeability and flow velocity at each of four strain levels. The damage within fractures leads to an increase in permeability. With an increase in external

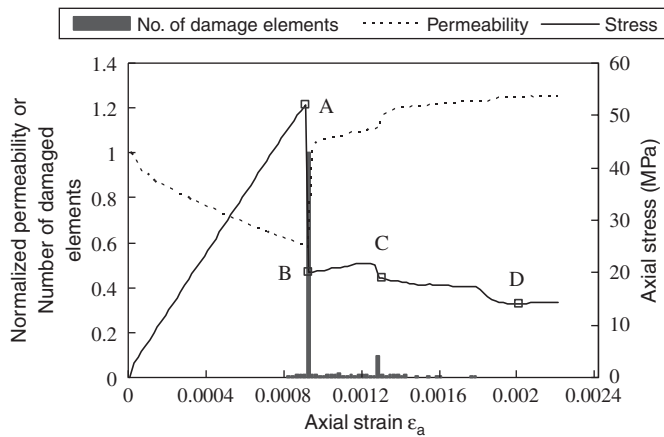


Fig. 16. The relationship among permeability, axial stress, number of damaged elements and axial strain under boundary condition BC-IV. The magnitude of permeability is normalized to its initial value of $5.4 \times 10^{-15} \text{ m}^2$, while the number of damage elements is also normalized to its maximum values of 1797.

displacement, these two damage zones become connected, and result in the formation of a preferential flow channel that is parallel to the direction of the applied hydraulic gradient.

By contrast, the flow velocity fields in the rock samples under these last two applied displacement boundary conditions are quite different from each other—due both to the existence of pre-existing fractures and to the newly formed macroscopic cracks. Before the peak stress is reached, although some cracks are also initiated in fractures, they do not link with each other to form new flow channels, therefore the overall permeability decreases monotonically even if these cracks have induced a local increase in permeability. At the post-peak region, the permeability increases obviously as a result the corresponding fluid flow patterns evolve from relatively uniform distributed porous flow, to highly focused flow along fractures. This phenomenon has been discussed in the previous studies [24,33]. In our simulation, the permeability of the damaged elements is specified to its 500 times; however, from these two simulations including flow process, it can be seen that the overall permeability increase is still very limited. Therefore, these simulation results denote that it is localization, together with its spatial arrangement, that dominates the overall hydro-mechanical behavior of the materials.

5. Conclusions

In this work, a DIB method is used to incorporate the characterization of rock heterogeneity directly into a well-established code named RFPA for the fully coupled hydromechanics of fractured rocks. This direct incorporation has made it possible to quantify the important impact of local rock heterogeneities on the coupled hydromechanical behavior of fractured rocks. This approach is

fundamentally different from the contemporary mathematical models in which statistical realizations are used to characterize the local rock heterogeneities. In statistical realization-based models, critical local-scale heterogeneities in rock may be overlooked because it is usually difficult to specify the statistical distribution of parameters that may fully represent the real microstructures of rock. In the DIB model presented here, the rock sample is discretized into many square elements, each of the same size, which directly correspond to the finite elements used to represent the mechanical and transport properties. Magnitudes of modulus and permeability may be assigned to elements, representative of the mineralogical composition based on DIB technique. A catalog of properties links the digital recognition with the appropriate mechanical or transport property. Using this technique, the basic governing equations are same for all components (i.e., minerals), but the material properties differ. The approach incorporates the small-scale variability in the initial deformation modulus, strength and permeability directly into a coupled hydro-mechanical model. In this DIB simulation approach, image voxels are mapped directly to equivalent mechanical and flow properties as defined by the voxel color or gray degree. These property maps are ported to the model capable of solving directly for the evolving deformation, and fluid flow. Because material properties can be resolved at pixel scales through the DIB processing technique, this approach can capture important heterogeneous effects which are crucially important for the coupled hydromechanics of fractured rocks.

Simulation examples demonstrate that depending on the loading conditions, the initial distribution patterns of rock heterogeneities, such as fractures, determine the coupled hydromechanical behaviors of fractured rocks. These behaviors include the coalescence of existing cracks, and the formation of new cracks. Subsequently, these behaviors would in turn affect the flow rate, stress redistribution, localized deformation and progressive failure process. In particular, we have graphically demonstrated that the pre-peak coupled hydromechanical responses are significantly different from those observed post-peak. In the pre-peak portion of the stress–strain curve, the permeability decreases with the axial stress and some cracks propagate from the existing fractures. However, these cracks do not coalesce to form flow-through channels. Therefore, the overall directional permeability is reduced monotonically with strain although the cracks may have induced local increases in permeability. In the post-peak regime, the cracks that form from existing fractures coalesce, and lead to unstable localized failure in the rock sample. Correspondingly, the permeability increases, and preferential flow channels are formed. These simulation results also demonstrate that it is localization, together with its spatial arrangement, that dominates the overall hydro-mechanical behavior of the materials.

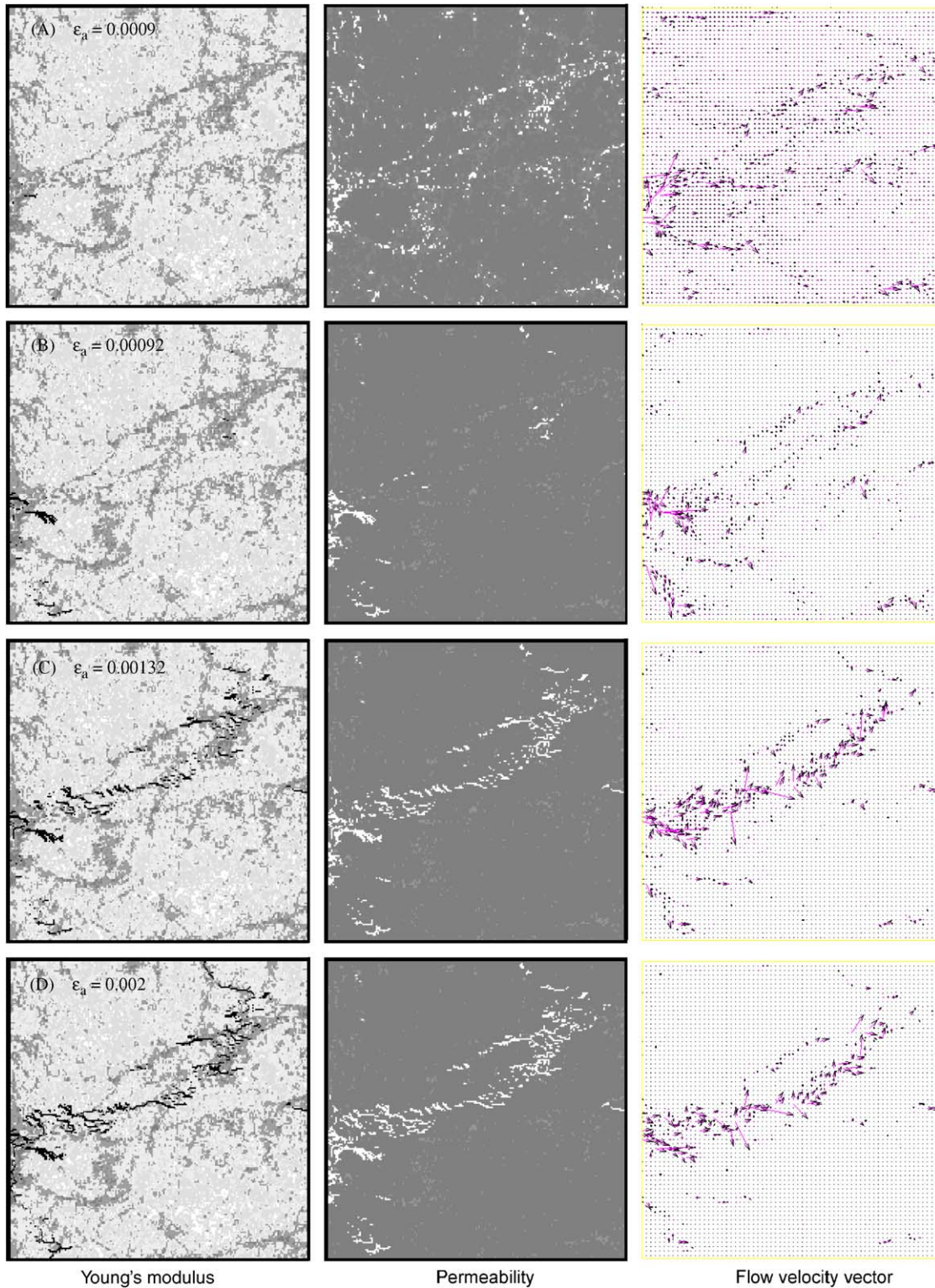


Fig. 17. The variation of Young's modulus, permeability and flow vector of rock sample under boundary condition BC-IV. The confining stress is 8.0 MPa, the hydraulic pressures at the top and bottom boundaries are 7.5 and 6.0 MPa, respectively, and ϵ_a is the axial strain in the horizontal direction.

Acknowledgments

This work is a result of partial support under grant ARC-DP0209425 and ARC-DP0342446, with additional

support provided to the first author by the Natural Science Foundation of China (Grant No. 50504005). This support is gratefully acknowledged.

References

- [1] Bower KM, Zvoloski GA. Numerical model for thermo-hydro-mechanical coupling in fractured rock. *Int J Rock Mech Min Sci* 1997;34(8):1201–11.
- [2] Tsang CF. Linking thermal, hydrological, and mechanical processes in fractured rocks. *Ann Rev Earth Planet Sci* 1999;27:359–84.
- [3] Rutqvist J, Stephansson O. The role of hydromechanical coupling in fractured rock engineering. *Hydrogeol J* 2003;11:7–40.
- [4] Neuman SP. Trends, prospects and challenges in quantifying flow and transport through fractured rocks. *Hydrogeol J* 2005;13:124–47.
- [5] Tang CA, Tham LG, Lee PKK, Yang TH, Li LC. Coupled analysis of flow, stress and damage (FSD) in rock failure. *Int J Rock Mech Min Sci* 2002;39:477–89.
- [6] Tang CA. Numerical simulation of progressive rock failure and associated seismicity. *Int J Rock Mech Min Sci* 1997;34:249–61.
- [7] Tang CA, Liu H, Lee PKK, Tsui Y, Tham LG. Numerical tests on micro-macro relationship of rock failure under uniaxial compression, part I: effect of heterogeneity. *Int J Rock Mech Min Sci* 2000;37:555–69.
- [8] Blair SC, Cook NGW. Analysis of compressive fracture in rock statistical techniques: Part I: A non-linear rule-based model. *Int J Rock Mech Min Sci* 1998;35:837–48.
- [9] Van Mier JGM. Fracture processes of concrete: assessment of material parameters for fracture models. Boca Raton, FL: CRC Press; 1997.
- [10] Zhu WC, Tang CA. Micromechanical model for simulating the fracture process of rock. *Rock Mech Rock Eng* 2004;37(1):25–56.
- [11] Hollister SJ, Kikuchi N. Homogenization theory and digital imaging: a basis for studying the mechanics and design principles of bone tissue. *Biotechnol Bioeng* 1994;43:586–96.
- [12] Takano N, Zako M, Kubo F, Kimura K. Microstructure-based stress analysis and evaluation for porous ceramics by homogenization method with digital image-based modeling. *Int J Solids Struct* 2003;40:1225–42.
- [13] Chermant JL. Why automatic image analysis? An introduction to this issue. *Cement Concr Compos* 2001;23:157–69.
- [14] Chung HC, Liang J, Kushiyama S, Shinozuka M. Digital image processing for non-linear system identification. *Int J Non-linear Mech* 2004;39:691–707.
- [15] Reid TR, Harrison JP. A semi-automated methodology for discontinuity trace detection in digital image of rock mass exposures. *Int J Rock Mech Min Sci* 2000;37:1073–89.
- [16] Santos LOE, Philippi PC, Damiani MC, Fernandes CP. Using three-dimensional reconstructed microstructures for predicting intrinsic permeability of reservoir rocks based on a Boolean lattice gas method. *J Petrol Sci Eng* 2002;35:109–24.
- [17] Hadjigeorgiou J, Lemy F, Cote P, Maldague X. An evaluation of image analysis algorithms for constructing discontinuity trace maps. *Rock Mech Rock Eng* 2003;36(2):163–79.
- [18] Daian J-F, Fernandes CP, Philippi PC, Bellini da Cunha Neto JA. 3D reconstitution of porous media from image processing data using a multiscale percolation system. *J Petrol Sci Eng* 2004;42:15–28.
- [19] Tham LG, Li L, Tsui Y, Lee PKK. A replica method for observing microcracks on rock surface. *Int J Rock Mech Min Sci* 2003;40:785–94.
- [20] Yue ZQ, Chen S, Tham LG. Finite element modeling of geomaterials using digital image processing. *Comput Geotech* 2003;30:375–97.
- [21] Yue ZQ, Morin I. Digital image processing for aggregate orientation in asphalt concrete mixtures. *Can J Civ Eng* 1996;23:479–89.
- [22] Chen S, Yue ZQ, Tham LG. Digital image-based numerical modelling method for prediction of inhomogeneous rock failure. *Int J Rock Mech Min Sci* 2004;41:939–57.
- [23] Yang TH, Tham LG, Tang CA, Liang ZZ, Tsui Y. Influence of heterogeneity of mechanical properties on hydraulic fracturing in permeable rocks. *Rock Mech Rock Eng* 2004;37(4):251–75.
- [24] Zhu W, Wong T-F. The transition from brittle faulting to cataclastic flow: permeability evolution. *J Geophys Res* 1997;102:3009–25.
- [25] Zoback MD, Byerlee JD. The effect of microcrack dilatancy on the permeability of Westerley granite. *J Geophys Res* 1975;80:752–5.
- [26] Brace WF. A note on permeability changes in geologic material due to stress. *Pure Appl Geophys* 1978;116:627–33.
- [27] Gonzalez RC, Woods RF. Digital image processing. Reading, MA: Addison-Wesley; 1992.
- [28] Lajtai EZ. Brittle fracture in compression. *Int J Fract* 1974;10(4):525–36.
- [29] Al-Wardy W, Zimmerman RW. Effective stress law for the permeability of clay-rich sandstones. *J Geophys Res* 2004;109(B04):B04203.
- [30] Brace WF, Bombolakis EG. A note on brittle crack growth in compression. *J Geophys Res* 1963;68:3709–13.
- [31] Hoek E, Bieniawski ZT. Brittle fracture propagation in rock under compression. *Int J Fract Mech* 1965;1:137–55.
- [32] Kranz RL. Crack–crack and crack–pore interactions in stressed granite. *Int J Rock Mech Min Sci* 1979;16:37–47.
- [33] Yuan SC, Harrison JP. Development of a hydro-mechanical local degradation approach and its application to modelling fluid flow during progressive fracturing of heterogeneous rocks. *Int J Rock Mech Min Sci* 2005;42(7–8):961–84.